NANO LETTERS
Cite This: Nano Lett. 2018, 18, 3792−3799
Letter
pubs.acs.org/NanoLett

Picosecond Quantum Cutting Generates Photoluminescence Quantum Yields Over 100% in Ytterbium-Doped $CsPbCl_3$ Nanocrystals

Tyler J. Milstein, Daniel M. Kroupa, and Daniel R. Gamelin*

Department of Chemistry, University of Washington, Seattle, Washington 98195, United States

Supporting Information

ABSTRACT: Recent advances in the ytterbium doping of $CsPbX_3$ (X = Cl or Cl/Br) nanocrystals have presented exciting new opportunities for their application as downconverters in solar-energy-conversion technologies. Here, we describe a hot-injection synthesis of Yb^{3+}:$CsPbCl_3$ nanocrystals that reproducibly yields sensitized Yb^{3+} $^2F_{5/2} \rightarrow {}^2F_{7/2}$ luminescence with near-infrared photoluminescence quantum yields (PLQYs) well over 100% and almost no excitonic luminescence. Near-infrared PLQYs of 170% have been measured. Through a combination of synthesis, variable-temperature photoluminescence spectroscopy, and transient-absorption and time-resolved photoluminescence spectroscopies, we show that the formation of shallow Yb^{3+}-induced defects play a critical role in facilitating a picosecond nonradiative energy-transfer process that de-excites the photoexcited nanocrystal and simultaneously excites two Yb^{3+} dopant ions, i.e., quantum cutting. Energy transfer is very efficient at all temperatures between 5 K and room temperature but only grows more efficient as the temperature is elevated in this range. Our results provide insights into the microscopic mechanism behind the extremely efficient sensitization of Yb^{3+} luminescence in $CsPbX_3$ nanocrystals, with ramifications for future applications of high-efficiency spectral-conversion nanomaterials in solar technologies.

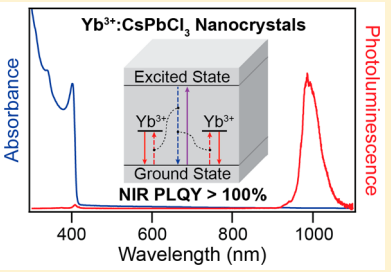

KEYWORDS: *Perovskite nanocrystals, quantum cutting, near-infrared emission, ytterbium doping, spectral downconversion*

All-inorganic, metal-halide perovskite $CsPbX_3$ (X = Cl, Br, or I) nanocrystals (NCs) have been the subject of intense recent research due to their high photoluminescence quantum yields (PLQY), narrow emission bandwidths, broadband absorption, and band gap tunability throughout the ultraviolet (UV), visible, and near-infrared (NIR) spectrum via size control (quantum size effects) and compositional alloying.[1−3] These properties have made perovskite NCs attractive materials for optoelectronic applications such as LEDs, lasing, displays, solar cells, and photodetectors.[4−6] The incorporation of impurity ions, or doping, in metal-halide perovskite NCs also imparts interesting optical properties. For example, substitutional B-site doping of $CsPbCl_3$ NCs with manganese ions (Mn^{2+}) gives rise to a broad, red-shifted emission band centered around 600 nm,[7−9] resulting from the NC sensitization of internal Mn^{2+} *d-d* emission. Very recently, successful doping of various trivalent lanthanide ions (or rare earths, RE) into colloidal perovskite NCs of $CsPbCl_3$ and $CsPbCl_{3(1-x)}Br_{3x}$ has been reported.[10,11] These materials display the rich, efficient, and inherently narrow luminescence features of the lanthanides sensitized by the perovskite NCs and have enabled promising proof-of-principle demonstration of down-conversion approaches to efficient solid-state lighting and solar photovoltaics.

Several publications have highlighted the attractiveness of Yb^{3+} as a luminescence activator for applications in solar spectral shifting and luminescent solar concentration.[10,12−15] Yb^{3+} has a simple electronic structure involving a single $^2F_{5/2}$ excited-state multiplet centered ∼1.3 eV above the $^2F_{7/2}$ ground state. This energy difference matches the bandgap of silicon (1.1 eV) well. Whereas extensive work has been done on Yb^{3+} doping of colloidal $NaYF_4$, LaF_3, and related insulator NCs, most intermediate- or narrow-gap colloidal semiconductor NCs possess soft anions that have low affinity for Yb^{3+}, and many possess tetrahedral cation sites that also disfavor Yb^{3+} incorporation. Sensitized NIR emission has been reported for colloidal Yb^{3+}-doped CdSe, $NaInS_2$, and $PbInS_4$ NCs, but the resulting NIR PLQYs were relatively small (<∼10%), limiting practical applications.[14,16] The successful synthesis of Yb^{3+}-doped $CsPbCl_3$ NCs thus addresses a long-standing challenge in nanocrystal chemistry. Remarkably, not only did this work demonstrate sensitization of Yb^{3+} luminescence by the NCs; it also described NIR PLQYs that exceeded 100%, attributed to quantum cutting. Yb^{3+} is a well-known activator for quantum cutting in bulk crystals, where the process is generally achieved via co-doping with other lanthanides such as Nd^{3+} or Pr^{3+}.[12,17,18] Very little is known about the structural or photophysical properties of Yb^{3+} dopants in perovskite NCs, however. Here, we apply a combination of synthesis and spectroscopic methods to examine the microscopic energy-transfer mechanism responsible for PLQYs > 100% in

Received: March 16, 2018
Revised: May 4, 2018
Published: May 10, 2018

DOI: 10.1021/acs.nanolett.8b01066
Nano Lett. 2018, 18, 3792−3799

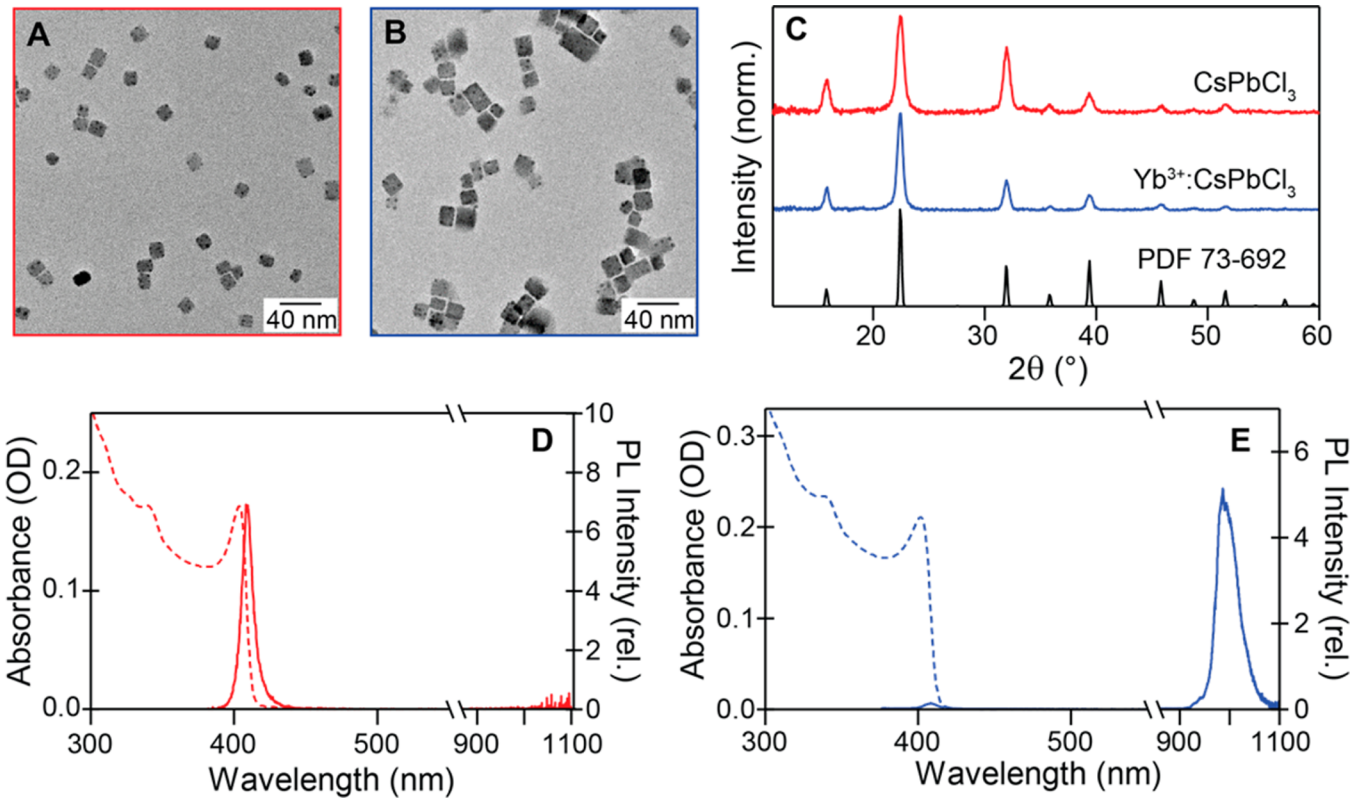

Figure 1. (a, b) TEM and (c) XRD data for undoped d = 13 nm $CsPbCl_3$ NCs (red) and d = 16 nm 6.0% Yb^{3+}:$CsPbCl_3$ NCs (blue). The dark spots in the TEM images result from in situ Pb^{2+} reduction by the electron beam, as commonly observed in $CsPbX_3$ NCs.[22] (d, e) Absorbance (dashed lines) and PL (solid lines) spectra of the same NCs. Yb^{3+} concentrations are defined as $[Yb^{3+}]/([Yb^{3+}] + [Pb^{2+}])$, measured analytically on the purified NCs by ICP-AES.

Yb^{3+}:$CsPbCl_3$ NCs. Comparisons between Yb^{3+} and Mn^{2+} luminescence activators in perovskite nanocrystals are also discussed.

In our hands, the synthesis of Yb^{3+}:$CsPbCl_3$ NCs following the methods described in refs 10 and 11 was met with some difficulties associated with poor precursor solubility (particularly $YbCl_3 \bullet 6H_2O$). We have therefore developed a hot-injection synthesis of colloidal $CsPbCl_3$ and Yb^{3+}:$CsPbCl_3$ NCs following the approach we previously introduced[19] for making Cs_2AgBiX_6 (X = Cl or Br) NCs, in which metal-acetate salts and chlorotrimethylsilane serve as the cation and halide precursors, respectively (see the Supporting Information for complete synthetic details). This synthetic route is attractive in part because of the high solubilities of the acetate precursors in high-boiling-point organic solvents compared to less-soluble chloride salts used in other popular syntheses.[19−21] Figure 1 summarizes general characterization data collected for representative undoped $CsPbCl_3$ NCs and (6%) Yb^{3+}-doped $CsPbCl_3$ NCs. The transmission electron microscopy (TEM) images in Figure 1a,b shows cubic crystallites with average edge lengths of approximately 13 and 16 nm for the undoped and Yb^{3+}-doped $CsPbCl_3$ NCs, respectively. Figure 1c shows X-ray diffraction (XRD) data collected from both samples, consistent with the perovskite crystal structure without detectable crystalline impurities. Negligible shifts of the XRD reflections are observed with Yb^{3+} doping, even at high Yb^{3+} concentrations. Figure 1d,e shows representative room-temperature absorption and steady-state PL spectra of undoped and Yb^{3+}-doped $CsPbCl_3$ NCs, respectively. The absorption spectra of both samples show similar onsets and peak positions. The PL spectrum of the undoped $CsPbCl_3$ NCs shows strong luminescence at 410 nm, corresponding to band-edge excitonic emission. In contrast, the PL spectrum of the Yb^{3+}:$CsPbCl_3$ NCs shows very little band-edge luminescence but intense NIR PL centered at 990 nm, corresponding to the $^2F_{5/2} \rightarrow {}^2F_{7/2}$ f-f emission of Yb^{3+}. The average lifetime of this Yb^{3+} emission is over 2 ms (see the Supporting Information), approaching its radiative limit and suggesting little nonradiative quenching of the emissive excited state. These data demonstrate successful synthesis of high-quality Yb^{3+}:$CsPbCl_3$ NCs.

To probe the effect of increasing the Yb^{3+} doping level, we performed a series of reactions under fixed conditions, varying only the nominal $[Yb^{3+}]$:$[Pb^{2+}]$ precursor ratio in the reaction mixture. We do not observe any appreciable changes in the $CsPbCl_3$ NC absorption spectrum with increasing Yb^{3+} concentration (see the Supporting Information), but both Yb^{3+} incorporation and Yb^{3+} luminescence intensity appear to increase with increasing Yb^{3+} precursor concentrations before peaking at a nominal $[Yb^{3+}]$:$[Pb^{2+}]$ ratio of ∼0.8 under these conditions and then decreasing again when this ratio is increased further (see Figure 2a and the Supporting Information). Upon analysis, we find a general trend of increasing NIR luminescence with increasing Yb^{3+} incorporation across the entire series, with some scatter. Figure 2b plots the excitonic and Yb^{3+} $^2F_{5/2} \rightarrow {}^2F_{7/2}$ absolute PLQYs measured using an integrating sphere (see the Supporting Information) versus the analytical Yb^{3+} concentration in the NCs. Excitonic PLQYs of the undoped samples are ∼20% and decrease sharply to <1% upon increasing the Yb^{3+} concentration to just ∼0.7% (see the Supporting Information for

DOI: 10.1021/acs.nanolett.8b01066
Nano Lett. 2018, 18, 3792−3799

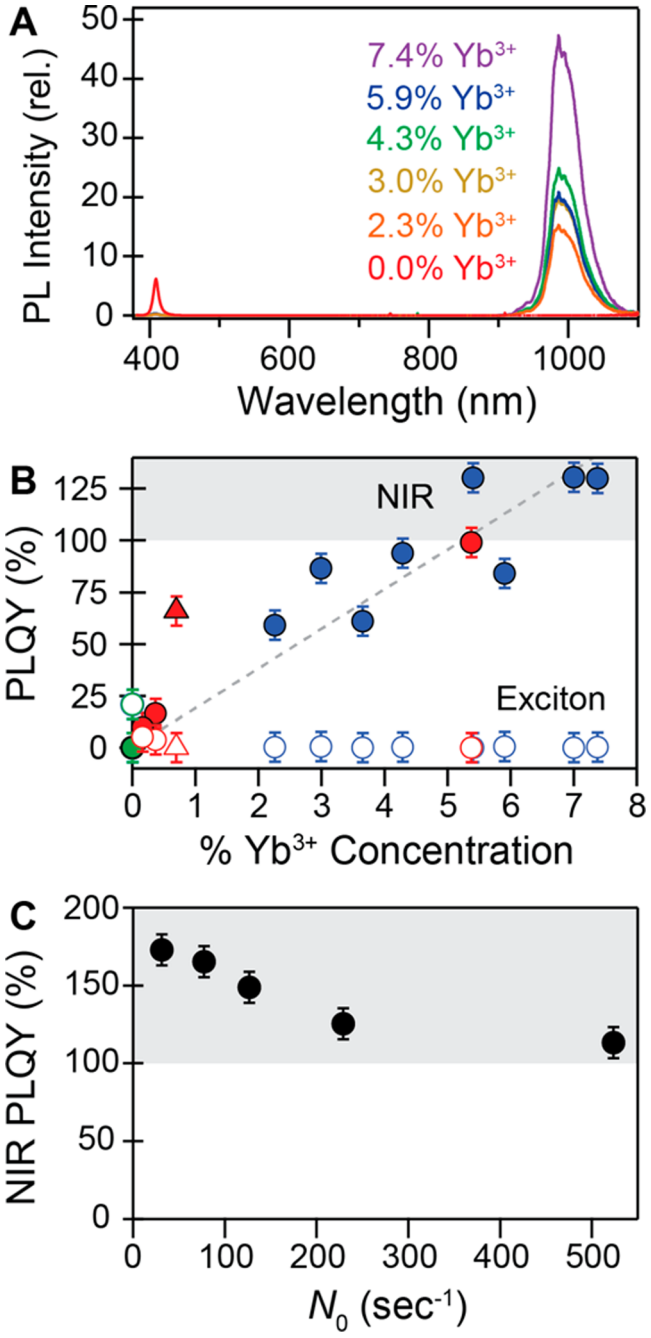

Figure 2. (a) Room-temperature PL spectra of colloidal $CsPbCl_3$ NCs (red) and Yb^{3+}:$CsPbCl_3$ NCs with analytical (nominal $[Yb^{3+}]:[Pb^{2+}]$) Yb^{3+}concentrations of 2.3% (0.1, orange), 3.0% (0.2, yellow), 4.3% (0.4, green), 5.9% (1.5, blue), and 7.4% (0.8, purple), all prepared with a fixed nominal ratio of $[Cs^+]:[Pb^{2+}] = 1.2$ in the reaction vessel. Yb^{3+} concentrations are defined as $[Yb^{3+}]/([Yb^{3+}] + [Pb^{2+}])$, measured analytically on the purified NCs by ICP-AES. (b) Exciton (open) and NIR (closed) PLQYs plotted as a function of Yb^{3+} concentration. λ_{ex} = 375 nm, CW excitation rate, $N_0 = 369\ s^{-1}$. The green data are from reactions without the addition of Yb^{3+} (undoped NCs). The blue data are from reactions varying the nominal Yb^{3+} concentrations at a fixed ratio of $[Cs^+]:[Pb^{2+}] = 1.4$. The red data are from additional reactions varying the nominal Cs^+ concentrations at a fixed ratio of $[Yb^{3+}]:[Pb^{2+}] = 0.2$. The data represented as triangles are from a reaction at the highest nominal $[Cs^+]:[Pb^{2+}]$, where a mixture of $CsPbCl_3$ and Cs_4PbCl_6 crystal phases is detected by XRD. (c) NIR PLQYs of a sample of 5.2% Yb^{3+}-doped $CsPbCl_3$ NCs plotted as a function of per-NC photoexcitation rate, tuned by varying the CW photoexcitation power at λ_{ex} = 380 nm. The experimental NIR PLQY reaches 170% at its highest value.

magnified data). Conversely, the Yb^{3+} $^2F_{5/2} \rightarrow {}^2F_{7/2}$ PLQYs increase roughly in proportion to the analytical doping concentration of Yb^{3+}, rising from 10 to 130% for 0.2 and 7.4% Yb^{3+}, respectively. At the highest Yb^{3+} doping level, we measure absolute PLQYs well above 100%, confirming this observation in recent reports.[11] The Cs^+ concentration in the reaction mixture was also found to affect both Yb^{3+} incorporation and the resulting NC optical properties (see the Supporting Information for details). Figure 2b includes additional excitonic and Yb^{3+} $^2F_{5/2} \rightarrow {}^2F_{7/2}$ PLQY data points obtained from reactions varying the nominal Cs^+ concentration, and these data follow the same trend lines as those obtained with $[Yb^{3+}]$ as the reaction variable, suggesting that the final Yb^{3+} concentration primarily dictates the resulting spectral properties.

Importantly, the PLQYs of these NCs are somewhat power-dependent, showing saturation effects even at relatively low excitation powers. Figure 2c plots the NIR PLQY for 5.2% Yb^{3+}-doped $CsPbCl_3$ NCs as a function of NC excitation rate. The PLQY increases from 110% up to 170% upon reducing the excitation rate by a factor of ~17. PL saturation occurs at these relatively low excitation rates because of the combination of the very large absorption cross-sections of the $CsPbCl_3$ NCs ($\sigma = 4.2 \times 10^{-14}$ cm^2 at 380 nm) with the long Yb^{3+} PL decay time (τ_{avg} > 2 ms; see the Supporting Information). This PL saturation reflects the introduction of a new nonradiative relaxation mechanism that only occurs upon photoexcitation of already-excited NCs. The PLQY of 170% measured here is the highest for any colloidal NC to date and is very close to the theoretical maximum of 200% for such a visible-to-NIR quantum cutting process involving Yb^{3+}.

Figure 3a plots the steady-state PL spectra of 7.4% Yb^{3+}:$CsPbCl_3$ NCs measured at several temperatures from 5 to 265 K. The excitonic PL is much weaker than the Yb^{3+} PL, but it is magnified here (12×) for clarity. At 5 K, the NIR region of the PL spectrum shows several resolved features characteristic of crystal-field splittings in the Yb^{3+} $^2F_{5/2} \rightarrow {}^2F_{7/2}$ emission. Increasing the temperature broadens these features, but the integrated intensities do not drop. Instead, whereas the excitonic PL intensity decreases rapidly as the temperature increases, the NIR Yb^{3+} $^2F_{5/2} \rightarrow {}^2F_{7/2}$ PL intensity only increases with increasing temperature. The onset temperature for this increase is ~50 K, possibly associated with the thermal excitation of vibrations. Figure 3b summarizes this temperature dependence by plotting the integrated excitonic and Yb^{3+} $^2F_{5/2} \rightarrow {}^2F_{7/2}$ PL intensities versus temperature. The NIR emission intensity actually triples upon increasing temperature from 5 to 265 K. The absorbance of these Yb^{3+}:$CsPbCl_3$ NCs at the excitation wavelength changes by <10% over this temperature range (see the Supporting Information). The integrated NIR PL is thus 10−200 times more intense than the excitonic PL at all temperatures. Overall, these data show efficient Yb^{3+} sensitization even at 5 K, and indicate that some aspect of the sensitization is thermally assisted. Importantly, these data show no evidence of thermally activated nonradiative decay of the luminescent Yb^{3+} excited state.

To probe the origins of this extremely efficient sensitized NIR luminescence in these Yb^{3+}:$CsPbCl_3$ NCs, we applied

DOI: 10.1021/acs.nanolett.8b01066
Nano Lett. 2018, 18, 3792−3799

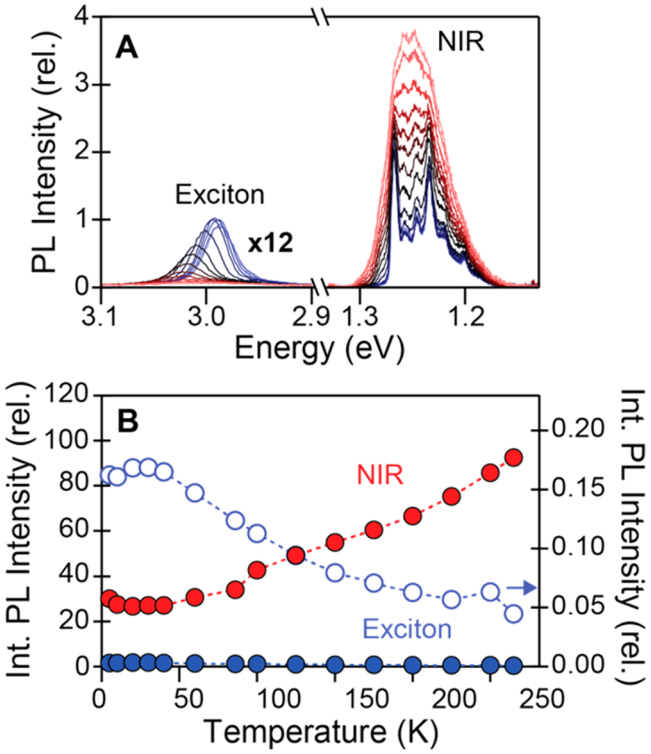

Figure 3. (a) Variable-temperature photoluminescence spectra of d = 16 nm 7.4% Yb^{3+}:$CsPbCl_3$ NCs, measured from 5 (light blue) to 280 K (pink). (b) Integrated NIR and excitonic PL intensities plotted vs temperature. The excitonic PL intensity is plotted both on same scale (closed circles) and on a magnified scale (open circles, ×550) as the NIR PL.

time-resolved spectroscopic techniques. Figure 4 compares room-temperature excitonic PL-decay and transient-absorption (TA) exciton bleach-recovery dynamics measured for a series of Yb^{3+}:$CsPbCl_3$ NCs with Yb^{3+} content ranging from 0−6%. The time-resolved PL (TRPL) data (Figure 4a) are limited at short times by an approximately 280 ps instrument response time, but at longer times, these data show nearly monoexponential decay with a time constant of ∼6 ns, associated with radiative decay of the exciton (τ_{rad}). The PL intensity of the slow component as a function of time [$I_S(t)$] can be fit by a monoexponential decay function at delay times, t, between 5 and 15 ns, defined by:

$$I_S(t) = A \exp[-t/\tau] \quad (1)$$

where A denotes the fitting amplitude and τ denotes the time constant. The amplitude of this slow decay component obtained from fitting the normalized PL decay curves is plotted versus Yb^{3+} concentration in Figure 4b. This amplitude decreases with increasing Yb^{3+} concentration, indicating a reduction in slow exciton PL with increasing Yb^{3+} doping. To obtain the amplitude of all fast PL decay (including decay that occurs faster than the instrument response time), we subtracted the slow component's amplitude from the normalized amplitude, which equals 1 at t = 0. The fast amplitudes are also plotted in Figure 4b. For comparison, Figure 4b further plots the ratio of steady-state NIR PL intensity to total PL intensity at each Yb^{3+} concentration: [I(NIR)/I(total)]. The fraction of fast PL decay roughly tracks this ratio at larger Yb^{3+} concentrations, but the data show that most of the effect of Yb^{3+} occurs faster than the instrument response (280 ps). These data thus suggest that Yb^{3+} excitation is associated with very rapid exciton depopulation.

TA data for the same series of Yb^{3+}:$CsPbCl_3$ NCs exhibit qualitatively similar trends but provide more information about short-time dynamics. TA spectra of these samples are all dominated by a bleach of the lowest-energy exciton transition, attributable to band-edge state filling upon photoexcitation (Figure 4c, inset; see the Supporting Information for a full data set). Figure 4c summarizes the excited-state dynamics for the various NC samples shown in Figure 4a, plotting TA amplitudes averaged over the full-width-at-half-maximum of this band-edge bleach feature versus time. These TA kinetics were fit using the kinetic model described by Wu et al. for $CsPbBr_3$ NCs (sum of exponentials weighted by their respective carrier contribution to the band-edge bleach signal; model details are given in the Supporting Information).[23] The fitting results agree well with those in ref 23 for the undoped NCs, and we modified the model to account for additional Yb^{3+}-based processes in the doped NCs. As in the TRPL, the amplitude of the slow component associated with radiative recombination (nanosecond time constants) systematically decreases with increasing Yb^{3+} content (Figure 4d), suggesting the introduction of new excited-state recombination pathways upon doping. Accordingly, two new fast-decay components (with sub-picosecond and ∼10 ps time constants) appear upon introduction of Yb^{3+} and increase in amplitude with increasing Yb^{3+} content (Figure 4d). These results verify the conclusion drawn from the TRPL analysis that Yb^{3+} doping introduces fast components in the exciton relaxation dynamics.

The dynamics and VTPL data allow analysis of the very high quantum yields in these samples. We take the NIR PL quantum yield to be:

$$\Phi_{\text{NIR PL}} = \frac{nk_{\text{ET}}}{(nk_{\text{ET}} + k_{\text{rad}} + k_{\text{tr}})} \times \Phi_{Yb^{3+}} \quad (2)$$

in which $\Phi_{Yb^{3+}}$ represents the internal luminescence QY of the Yb^{3+} activators and ET, rad, and tr and denote energy transfer to Yb^{3+}, radiative band-edge recombination, and carrier trapping, respectively. Increasing n (the number of optically active Yb^{3+} activators) results in a higher NIR PLQY as the branching ratio approaches unity. $\Phi_{Yb^{3+}}$ itself is inherently large, as determined from the VTPL data in which the NIR emission shows no thermal quenching when the temperature is increased toward room temperature. Interestingly, despite the rapid and efficient energy transfer in combination with the fast carrier trapping, excitonic luminescence is still observed. We understand this to be the result of a small n (see the Supporting Information for details and discussion).

It is instructive to compare Yb^{3+} and Mn^{2+} as luminescence activators in perovskite NCs. Although both activator ions can have very high internal quantum efficiencies for luminescence, the highest PLQYs of the Yb^{3+}:$CsPbCl_3$ NCs (170%, Figure 2c) are almost three times as large as the highest PLQYs observed from Mn^{2+}:$CsPbCl_3$ NCs to date (up to 60%).[7−9,24] Furthermore, energy transfer from the NCs to Yb^{3+} is not suppressed at cryogenic temperatures, nor is it too slow to compete with exciton recombination despite the fact that exciton recombination accelerates to sub-nanosecond time scales at low temperatures. These characteristics contrast those of Mn^{2+}:$CsPbCl_3$ NCs, whose luminescence is completely dominated by excitonic emission at low temperatures because energy transfer to Mn^{2+} is too slow to compete with exciton

DOI: 10.1021/acs.nanolett.8b01066
Nano Lett. 2018, 18, 3792−3799

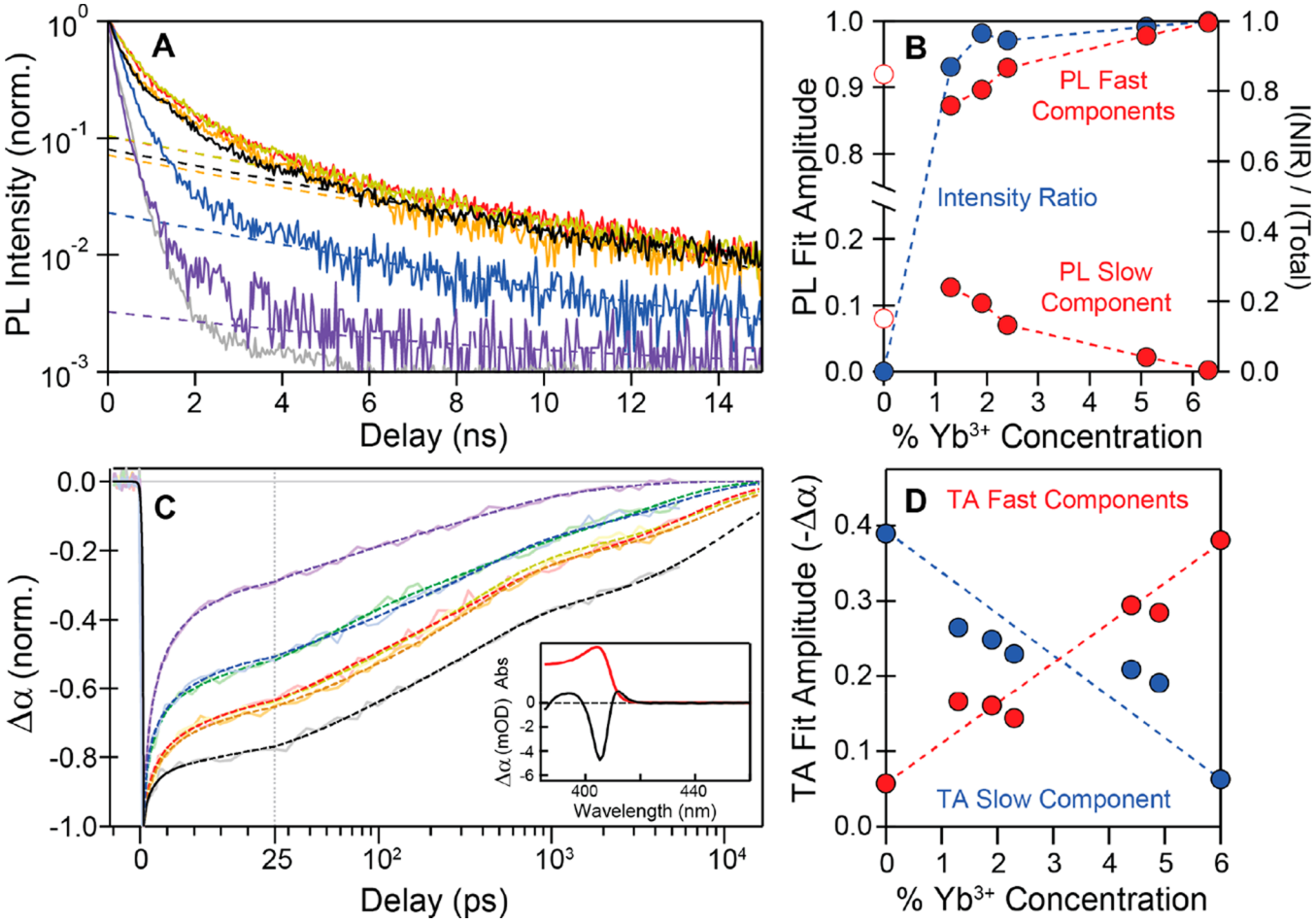

Figure 4. (a) Room-temperature TRPL decay traces for undoped (black trace) and Yb^{3+}-doped (red to purple) $CsPbCl_3$ NCs. The instrument response function (IRF) is also plotted (gray). The IRF curve is shifted downward by 10^{-3} for clarity of the logarithmic presentation. (b) Fast and slow PL decay amplitudes (red) and PL intensity ratio (blue) plotted vs analytical Yb^{3+} concentration. (c) First-exciton bleach-recovery kinetics measured at room temperature. Inset: representative absorption and transient-absorption spectra at the $CsPbCl_3$ NC absorption edge showing the negative first-exciton bleach signal. (d) Fast (red) and slow (blue) TA amplitudes plotted vs analytical Yb^{3+} concentration.

recombination at these temperatures. Energy transfer to Mn^{2+} in $CsPbCl_3$ NCs likely proceeds via a resonant Dexter-type energy-transfer process involving the NC exciton and an upper ligand-field excited state of Mn^{2+} at the same energy.[9] This energy matching along with the fact that Mn^{2+} experiences greater covalency with the surrounding lattice should give rise to much larger electronic coupling and hence greater Dexter energy-transfer rates compared to Yb^{3+}, which has poor electronic coupling and no upper excited states at the energy of the $CsPbCl_3$ exciton. Thus, if energy transfer to Yb^{3+} proceeded by an analogous Dexter-type mechanism, it should be much slower and not much faster, as was observed. Energy transfer to Mn^{2+} occurs on the time scale of hundreds of picoseconds to nanoseconds, but energy transfer to Yb^{3+} appears to occur on the time scale of 1 ps. Indeed, exciton depopulation leading to Yb^{3+} sensitization is so fast that it is competitive with other fast carrier-trapping processes active even in undoped $CsPbCl_3$ NCs, e.g., as illustrated from their TA kinetics (sub-picosecond and ~2 ps for the hole- and electron-trapping time constants, respectively). Such fast energy transfer to Yb^{3+} appears incommensurate with the known characteristics of Yb^{3+} as a luminescence activator. This inconsistency suggests that energy transfer to Yb^{3+} must occur via an alternative route rather than by normal exciton-dopant Dexter-type energy transfer.

We propose that the extremely fast exciton depopulation observed in these Yb^{3+}:$CsPbCl_3$ NCs, in conjunction with the correlation between Yb^{3+} doping and NIR PLQYs, implies the integral participation of lattice defects in the Yb^{3+} sensitization mechanism. Moreover, to achieve the extraordinary PLQYs of as high as ~170%, this sensitization mechanism must involve quantum cutting. To account for these considerations, we hypothesized that Yb^{3+} doping itself introduces correlated defects that rapidly localize excitation energy in the vicinity of the Yb^{3+} activators. Picosecond energy localization by such a defect would then be followed by energy transfer from that defect to a pair of neighboring Yb^{3+} ions, resulting in the emission of two NIR photons, i.e., quantum cutting. This process would be manifested in eq 2 as multiplication of the branching ratio by a factor of 2. If this hypothesis is correct, such defects are likely associated with the aliovalent charge of Yb^{3+} in the $CsPbCl_3$ lattice, which requires charge compensation.

To test for such a dopant-induced lattice defect, we doped $CsPbCl_3$ NCs with La^{3+} cations using the same methods employed to synthesize the Yb^{3+}:$CsPbCl_3$ NCs. La^{3+} is optically inert but still aliovalent, and it has the same charge-

DOI: 10.1021/acs.nanolett.8b01066
Nano Lett. 2018, 18, 3792−3799

compensation requirements as Yb^{3+}. Figure 5a shows the PL spectra of 1.3% La^{3+}:$CsPbCl_3$ NCs collected at 4.7 and 223 K.

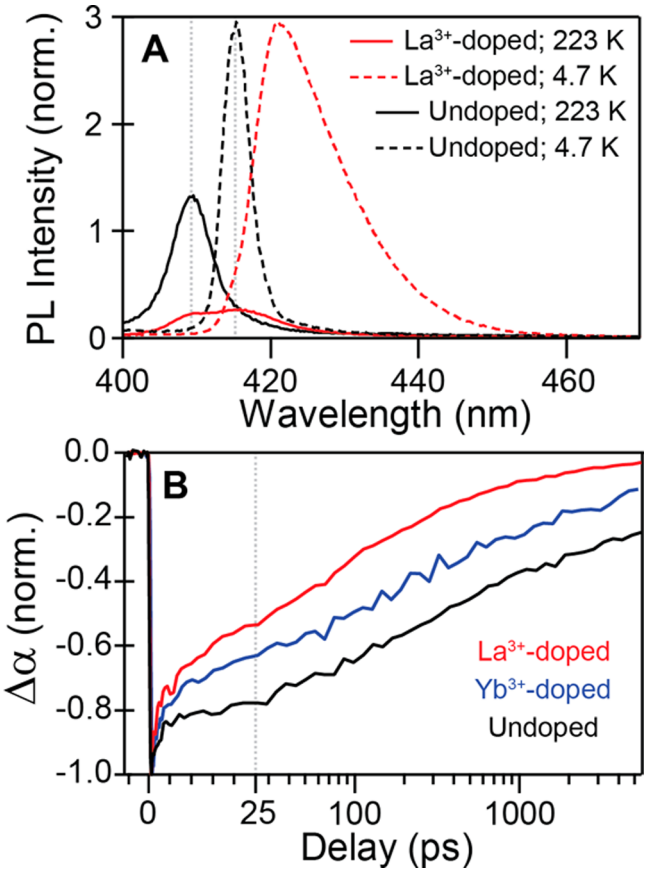

Figure 5. (a) Variable temperature PL of 1.3% La^{3+}-doped (red) and undoped (black) $CsPbCl_3$ NCs at 4.7 K (dashed) and 223 K (solid) under 375 nm excitation. (b) TA bleach-recovery kinetics of undoped (black), 1.3% La^{3+}-doped (red), and 1.3% Yb^{3+}-doped (blue) $CsPbCl_3$ NCs.

For comparison, Figure 5a also plots parallel data collected for undoped $CsPbCl_3$ NCs. At 4.7 K, the La^{3+}:$CsPbCl_3$ NCs indeed show a prominent, broad PL feature indicative of shallow-trap emission. This feature peaks ~40 meV below the excitonic PL of the undoped $CsPbCl_3$ NCs. No other emission is observed from the La^{3+}:$CsPbCl_3$ NCs. A similar trap PL band has been reported for La^{3+}:$CsPbCl_3$ single crystals,[25] suggesting that this is an internal lattice defect not associated with the NC surfaces. This trap luminescence in these La^{3+}:$CsPbCl_3$ NCs is very bright below ~80 K, but increasing the temperature above ~80 K causes excitonic PL to grow in at the expense of the broad trap PL, and the overall PL decreases substantially (see the Supporting Information for additional data). The trap PL is still observed at the highest temperature in this series (223 K), and it is also observed at room temperature. At cryogenic temperature, ~99% of this trap PL decays within ~300 ps, with the remaining ~1% decaying at a slower rate (see the Supporting Information). The observation of near-band-edge trap PL in the La^{3+}:$CsPbCl_3$ NCs provides strong support for the hypothesis of a shallow dopant-induced defect state introduced when trivalent cations are doped into $CsPbCl_3$ NCs.

This conclusion is bolstered by TA studies of the La^{3+}:$CsPbCl_3$ NCs. Figure 5b shows TA bleach-recovery kinetics measured for undoped, Yb^{3+}-doped, and La^{3+}-doped $CsPbCl_3$ NC samples. Similar to the Yb^{3+}:$CsPbCl_3$ NC data, the La^{3+}:$CsPbCl_3$ NC kinetic trace is fit well using two additional fast bleach-recovery components (sub-picosecond and ~10 ps time constants) relative to the undoped $CsPbCl_3$ NCs, suggesting that both trivalent dopants introduce similar trapping defects.

The above information now allows a mechanism underlying the extremely efficient sensitization of NIR PL in Yb^{3+}:$CsPbCl_3$ NCs to be proposed. The data suggest that Yb^{3+} doping introduces a charge-compensating defect that acts as a shallow trap. This defect localizes excitation energy on the picosecond time scale. Charge compensation could be manifested as a cation vacancy (V_{Cs} or V_{Pb}) or the loss of a surface oleylammonium ligand. Previous computational work characterizing possible common defects and their energies relative to the band edges in $CsPbBr_3$ has shown that V_{Cs} and V_{Pb} are both shallow traps,[26] which would be consistent with the relatively small energy difference between excitonic and trap-induced defect PL seen in Figure 5. The energies of such traps relative to the band edges of $CsPbCl_3$ are unknown, however, as is the influence of a neighboring trivalent cation on these energies. To be consistent with the observation of efficient quantum cutting, we propose that the relevant defect is a V_{Pb} within a charge-neutral M^{3+}-V_{Pb}-M^{3+} defect complex. In fact, an analogous charge-compensating motif is already well-documented in $CsCdBr_3$ and related halide lattices, in which it is known as a "McPherson pair".[27,28] Although the crystal structure of those materials differs from the perovskite structure, an analogous defect complex appears reasonable here. Additionally, V_{Pb} rather than V_{Cs} formation is consistent with our experimental observation that the NIR PLQY actually increases with increasing nominal Cs^+ concentration during synthesis, a condition that should disfavor V_{Cs} formation. Carrier capture by V_{Pb} within a Yb^{3+}-V_{Pb}-Yb^{3+} defect complex localizes this defect excited state in close proximity to two Yb^{3+} cations simultaneously; this localization enables energy transfer to both Yb^{3+} ions in a concerted quantum-cutting step. The La^{3+}-induced defect emission exceeds only slightly the energy required for simultaneous excitation of both neighboring Yb^{3+} ions. This PL intensity is nearly zero at exactly twice the energy of the highest Yb^{3+} $^2F_{5/2}$-$^2F_{7/2}$ crystal-field absorption feature in this lattice (~2.56 eV), but this energy gap is easily bridged by a few lattice phonons. Importantly, because this defect-state population decays within ~300 ps in the analogous La^{3+}:$CsPbCl_3$ NCs, energy transfer from this state to Yb^{3+} must occur even faster than this, i.e., this quantum cutting occurs on a picosecond time scale.

Scheme 1 summarizes these mechanistic conclusions. Scheme 1a illustrates the formation of a dopant-induced shallow defect level upon incorporation of trivalent impurity ions into the $CsPbCl_3$ lattice. This new defect level is able to compete with native defects for capture of photogenerated carriers. It is proposed as a charge-neutral M^{3+}-V_{Pb}-M^{3+} defect complex. When the trivalent dopant is spectroscopically innocent, such as La^{3+}, the formation of this defect is manifested as near-band-edge PL. Scheme 1b illustrates how this scenario changes when the trivalent defect is Yb^{3+}. In this case, formation of the trapped excited state is followed by nearly resonant energy transfer to form two excited Yb^{3+} ions in a single, concerted, quantum-cutting step. Quantum cutting is aided by the fact that the proposed V_{Pb} defect is always in close proximity to two Yb^{3+} ions because of its role in their charge compensation. This proximity provides sufficient electronic

DOI: 10.1021/acs.nanolett.8b01066
Nano Lett. 2018, 18, 3792−3799

Scheme 1. Proposed (a) La^{3+}-Induced Defect Emission Process, (b) Yb^{3+}-Sensitization Mechanism Involving an Analogous Yb^{3+}-Induced Defect State, and (c) the Proposed Charge-Neutral Vacancy-Defect Structure Arising from Doping $CsPbCl_3$ NCs with Trivalent Cations

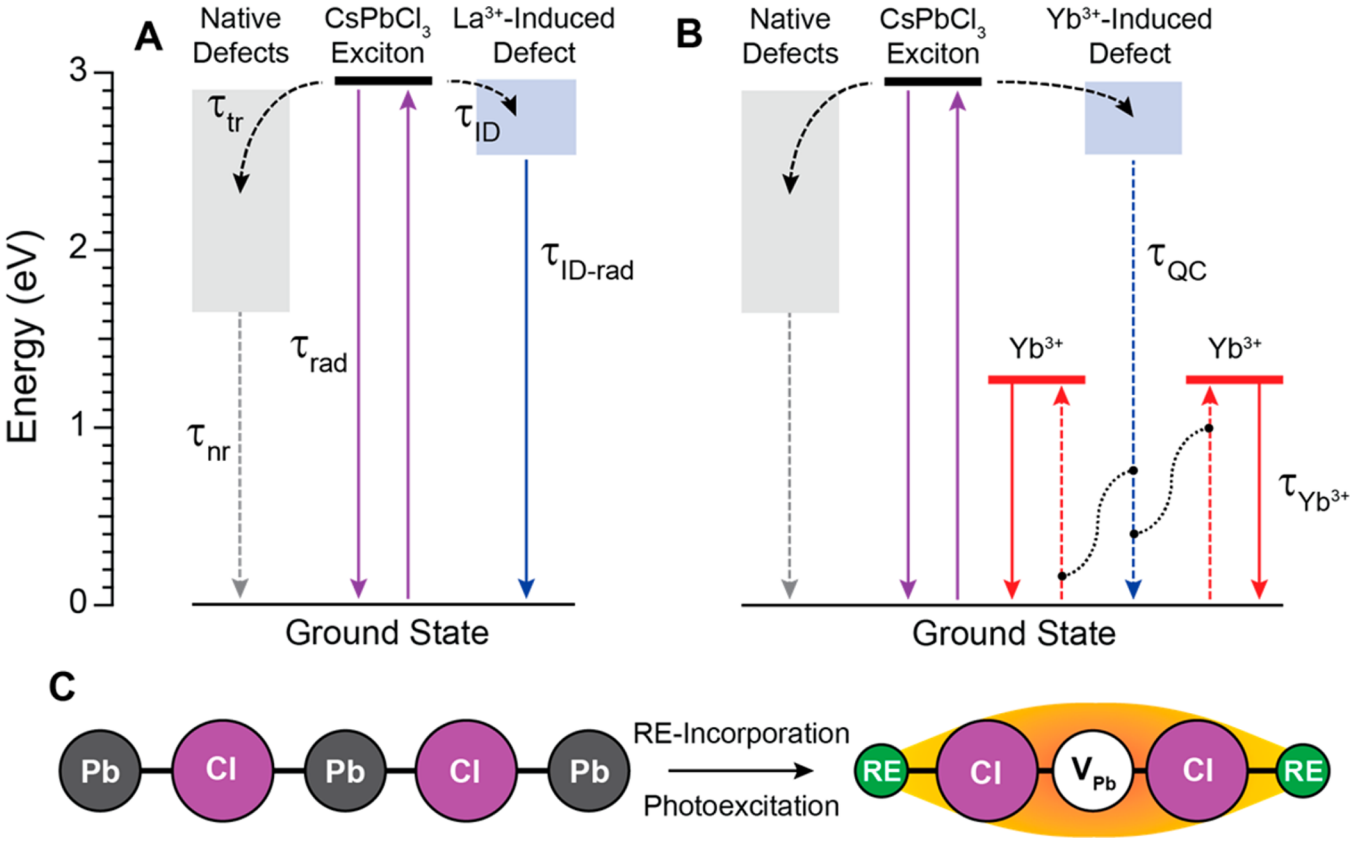

coupling to both Yb^{3+} ions for efficient simultaneous excitation of both. As a shallow defect, V_{Pb}-localized photogenerated charge carriers will have a large Bohr radius, aiding electronic coupling to both Yb^{3+} ions simultaneously (Scheme 1c). This proposed mechanism differs from the one suggested previously to explain quantum cutting in Yb^{3+}:$CsPbCl_3$ NCs,[11] which involves decay of a band-edge photogenerated electron to a defect state coupled to excitation of a single Yb^{3+} ion, with subsequent electron decay from the defect state to the valence band releasing another quantum of energy to excite a second Yb^{3+} ion. Our data provide direct evidence for formation of a shallow dopant-induced defect state in these materials, and in the absence of any other detectable midgap states in these NCs, this result strongly suggests that sensitization occurs via simultaneous excitation of Yb^{3+} pairs, as illustrated in Scheme 1b. We note that the integral role of a specific defect implied by Scheme 1 is consistent with the otherwise unusual observation that very high Yb^{3+} concentrations are needed to fully quench excitonic PL in these Yb^{3+}:$CsPbCl_3$ NCs despite picosecond exciton depopulation kinetics. This apparent inconsistency is explained by the need for a specific Yb^{3+}-V_{Pb}-Yb^{3+} defect complex to achieve not just quantum cutting but also Yb^{3+} sensitization. In the absence of such a well-positioned (energetically and spatially) defect, exciton-to-Yb^{3+} energy transfer is expected to be very slow (much slower than Mn^{2+}) because of poor electronic coupling and a large energy mismatch.

In conclusion, high-quality Yb^{3+}:$CsPbCl_3$ NCs have been synthesized via a novel hot-injection route starting from the respective metal-acetate salts and halide precursors. These NCs show analytical Yb^{3+} concentrations as high as 7.5% and replicable PLQYs exceeding 100%, reaching as high as ~170%. These extremely high PLQYs are shown to result from energy capture by a Yb^{3+}-induced defect that subsequently transfers its energy to two neighboring Yb^{3+} ions in a single concerted step on the picosecond time scale. The above-unity quantum yields of these materials make them very promising for numerous photonic applications, from photodetection to solar energy conversion. The results presented here provide insights into the origins of this unique photophysical property and further advance the development of Yb^{3+}-doped perovskite nanocrystals for such applications.

■ ASSOCIATED CONTENT

Supporting Information

The Supporting Information is available free of charge on the ACS Publications website at DOI: 10.1021/acs.nanolett.8b01066.

Additional experimental details and discussion, XRD data, absorption spectra, PL lifetime data, variable-temperature excitonic PL, absorption data, and kinetic models (PDF)

■ AUTHOR INFORMATION

Corresponding Author

*E-mail: gamelin@chem.washington.edu.

ORCID

Tyler J. Milstein: 0000-0002-1517-2222

Daniel M. Kroupa: 0000-0002-2788-3670

DOI: 10.1021/acs.nanolett.8b01066
Nano Lett. 2018, 18, 3792−3799

Daniel R. Gamelin: 0000-0003-2888-9916

Notes

The authors declare no competing financial interest.

■ ACKNOWLEDGMENTS

This research was supported by the U.S. National Science Foundation (grants no. DMR-1505901 and no. DMR-1807394 to D.R.G.) and by the State of Washington through the University of Washington Clean Energy Institute (to T.J.M.), including via funding from the Washington Research Foundation (to D.M.K.). This research was partially supported by the U.S. National Science Foundation through the University of Washington Molecular Engineering Materials Center, a Materials Research Science and Engineering Center (grant no. DMR-1719797). Part of this work was conducted at the Molecular Analysis Facility, a National Nanotechnology Coordinated Infrastructure site at the University of Washington that is supported in part by the National Science Foundation (grant no. ECC-1542101), the University of Washington, the Molecular Engineering & Sciences Institute, the Clean Energy Institute, and the National Institutes of Health. Michael De Siena is acknowledged for acquiring the TEM images. Dr. Sidney Creutz is acknowledged for helpful discussion.

■ REFERENCES

(1) Protesescu, L.; Yakunin, S.; Bodnarchuk, M. I.; Krieg, F.; Caputo, R.; Hendon, C. H.; Yang, R. X.; Walsh, A.; Kovalenko, M. V. *Nano Lett.* **2015**, *15*, 3692−3696.
(2) Nedelcu, G.; Protesescu, L.; Yakunin, S.; Bodnarchuk, M. I.; Grotevent, M. J.; Kovalenko, M. V. *Nano Lett.* **2015**, *15*, 5635−5640.
(3) Protesescu, L.; Yakunin, S.; Kumar, S.; Bär, J.; Bertolotti, F.; Masciocchi, N.; Guagliardi, A.; Grotevent, M.; Shorubalko, I.; Bodnarchuk, M. I.; Shih, C.-J.; Kovalenko, M. V. *ACS Nano* **2017**, *11*, 3119−3134.
(4) Zhang, F.; Zhong, H.; Chen, C.; Wu, X.-g.; Hu, X.; Huang, H.; Han, J.; Zou, B.; Dong, Y. *ACS Nano* **2015**, *9*, 4533−4542.
(5) Swarnkar, A.; Marshall, A. R.; Sanehira, E. M.; Chernomordik, B. D.; Moore, D. T.; Christians, J. A.; Chakrabarti, T.; Luther, J. M. *Science* **2016**, *354*, 92.
(6) Kim, Y.-H.; Wolf, C.; Kim, Y.-T.; Cho, H.; Kwon, W.; Do, S.; Sadhanala, A.; Park, C. G.; Rhee, S.-W.; Im, S. H.; Friend, R. H.; Lee, T.-W. *ACS Nano* **2017**, *11*, 6586−6593.
(7) Liu, W.; Lin, Q.; Li, H.; Wu, K.; Robel, I.; Pietryga, J. M.; Klimov, V. I. *J. Am. Chem. Soc.* **2016**, *138*, 14954−14961.
(8) Parobek, D.; Roman, B. J.; Dong, Y.; Jin, H.; Lee, E.; Sheldon, M.; Son, D. H. *Nano Lett.* **2016**, *16*, 7376−7380.
(9) Yuan, X.; Ji, S.; De Siena, M. C.; Fei, L.; Zhao, Z.; Wang, Y.; Li, H.; Zhao, J.; Gamelin, D. R. *Chem. Mater.* **2017**, *29*, 8003−8011.
(10) Zhou, D.; Liu, D.; Pan, G.; Chen, X.; Li, D.; Xu, W.; Bai, X.; Song, H. *Adv. Mater.* **2017**, *29*, 1704149.
(11) Pan, G.; Bai, X.; Yang, D.; Chen, X.; Jing, P.; Qu, S.; Zhang, L.; Zhou, D.; Zhu, J.; Xu, W.; Dong, B.; Song, H. *Nano Lett.* **2017**, *17*, 8005−8011.
(12) Meijer, J.-M.; Aarts, L.; van der Ende, B. M.; Vlugt, T. J. H.; Meijerink, A. *Phys. Rev. B: Condens. Matter Mater. Phys.* **2010**, *81*, 035107.
(13) Erickson, C. S.; Bradshaw, L. R.; McDowall, S.; Gilbertson, J. D.; Gamelin, D. R.; Patrick, D. L. *ACS Nano* **2014**, *8*, 3461−3467.
(14) Creutz, S. E.; Fainblat, R.; Kim, Y.; De Siena, M. C.; Gamelin, D. R. *J. Am. Chem. Soc.* **2017**, *139*, 11814−11824.
(15) van der Ende, B. M.; Aarts, L.; Meijerink, A. *Phys. Chem. Chem. Phys.* **2009**, *11*, 11081−11095.
(16) Martín-Rodríguez, R.; Geitenbeek, R.; Meijerink, A. *J. Am. Chem. Soc.* **2013**, *135*, 13668−13671.
(17) van der Ende, B. M.; Aarts, L.; Meijerink, A. *Adv. Mater.* **2009**, *21*, 3073−3077.
(18) Liu, L.; Li, M.; Cai, S.; Yang, Y.; Mai, Y. *Opt. Mater. Express* **2015**, *5*, 756−763.
(19) Creutz, S. E.; Crites, E. N.; De Siena, M. C.; Gamelin, D. R. *Nano Lett.* **2018**, *18*, 1118−1123.
(20) Imran, M.; Caligiuri, V.; Wang, M.; Goldoni, L.; Prato, M.; Krahne, R.; De Trizio, L.; Manna, L. *J. Am. Chem. Soc.* **2018**, *140*, 2656−2664.
(21) Krieg, F.; Ochsenbein, S. T.; Yakunin, S.; ten Brinck, S.; Aellen, P.; Süess, A.; Clerc, B.; Guggisberg, D.; Nazarenko, O.; Shynkarenko, Y.; Kumar, S.; Shih, C.-J.; Infante, I.; Kovalenko, M. V. *ACS Energy Lett.* **2018**, *3*, 641−646.
(22) Dang, Z.; Shamsi, J.; Palazon, F.; Imran, M.; Akkerman, Q. A.; Park, S.; Bertoni, G.; Prato, M.; Brescia, R.; Manna, L. *ACS Nano* **2017**, *11*, 2124−2132.
(23) Wu, K.; Liang, G.; Shang, Q.; Ren, Y.; Kong, D.; Lian, T. *J. Am. Chem. Soc.* **2015**, *137*, 12792−12795.
(24) Xu, K.; Lin, C. C.; Xie, X.; Meijerink, A. *Chem. Mater.* **2017**, *29*, 4265−4272.
(25) Watanabe, K.; Koshimizu, M.; Yanagida, T.; Fujimoto, Y.; Asai, K. *Jpn. J. Appl. Phys.* **2016**, *55*, 02BC20.
(26) Kang, J.; Wang, L.-W. *J. Phys. Chem. Lett.* **2017**, *8*, 489−493.
(27) Henling, L. M.; McPherson, G. L. *Phys. Rev. B* **1977**, *16*, 4756−4760.
(28) McPherson, G. L.; Henling, L. M. *Phys. Rev. B* **1977**, *16*, 1889−1892.

DOI: 10.1021/acs.nanolett.8b01066
Nano Lett. 2018, 18, 3792−3799